Research Square

Preprints are preliminary reports that have not undergone peer review.
They should not be considered conclusive, used to inform clinical practice,
or referenced by the media as validated information.

MnOx/g-C_3N_4 heterostructure Modified Pervious Concrete for Enhanced Visible-Light Photocatalytic Degradation of Rhodamine B

Xuelu Xu

xueluxu@sut.edu.cn

Shenyang University of Technology

Yue Dong

Shenyang University of Technology

Sijin Zhang

Shenyang University of Technology

Shuai Yang

Shenyang University of Technology

Jin Meng

Shenyang University of Technology

Jie Huang

Shenyang University of Technology

Lili Jiang

Shenyang University of Technology

Article

Keywords: g-C_3N_4, MnO□, heterostructure, photocatalysis, Rhodamine B, pervious concrete

Posted Date: November 10th, 2026

DOI: https://doi.org/10.21203/rs.3.rs-11391640/v1

License: This work is licensed under a Creative Commons Attribution 4.0 International License.
Read Full License

Additional Declarations: No competing interests reported.

MnO_x/g-C_3N_4 heterostructure Modified Pervious Concrete for Enhanced Visible-Light Photocatalytic Degradation of Rhodamine B

Xuelu Xu[a,*], Yue Dong[a], Sijin Zhang[b], Shuai Yang[a], Jin Meng[a], Jie Huang[a], Lili Jiang[a,*]

(a School of College of Architecture and Civil Engineering, Shenyang University of Technology, Shenyang 110870, P. R. China)

(b School of Materials Science and Engineering, Shenyang University of Technology, Shenyang 110870, P. R. China)

*Corresponding author
**Corresponding author
E-mail addresses: xueluxu@sut.edu.cn, 57386764@qq.com

Abstract:

Graphitic carbon nitride (g-C_3N_4) represents a promising metal-free visible-light-responsive photocatalyst for organic wastewater remediation. However, rapid recombination of photogenerated carriers and inadequate visible-light harvesting severely limit its practical environmental applications. Herein, MnO_x/g-C_3N_4 heterostructured composites were fabricated by a one-step thermal method to promote charge separation and enhance visible-light utilization. The photocatalytic activity of the catalysts was further assessed by degradation of Rhodamine B (RhB) under visible-light irradiation. The optimized Mn-$GCN_{700\text{-}3:2}$ achieved 99.83% RhB degradation within 60 min, 49.51% higher than pristine GCN_{700}, which showed 75.57% degradation after 120 min, and retained 90.13% efficiency after six cycles. All the samples were subjected to comprehensive characterizations (XRD, XPS, SEM, TEM, FT-IR, UV-vis DRS and PL). XPS analysis revealed that Mn^{3+} accounted for 70% of the Mn species, forming a mixed-valence Mn^{3+}/Mn^{4+} system, while FT-IR confirmed strong interfacial coupling between MnO_x and g-C_3N_4. UV-vis DRS, bandgap, and PL analyses demonstrated that Mn incorporation markedly narrowed the bandgap, enhanced visible-light absorption, and suppressed charge recombination. The Mn^{3+}/Mn^{4+} redox cycle acted as electron traps to promote charge separation and O_2 activation into $\cdot O_2^-$, which cooperated with ·OH and h^+ to drive efficient RhB degradation. When immobilized on pervious concrete at 5 g/L (MnPC), the degradation of RhB achieved 78.11% within 120 min under visible light, outperforming GPC and satisfying the *Technical Specification for Pervious Cement Concrete Pavement*. This work proposes a facile route to synthesize high-efficiency photocatalysts and spray on pervious concrete, which provides a sustainable technical candidate for decentralized urban stormwater and wastewater purification.

Keywords: g-C_3N_4; MnO_x; heterostructure; photocatalysis; Rhodamine B; pervious concrete;

1 Introduction

The development of effective and sustainable pollution control methods has become increasingly critical in recent years due to severe organic water pollution caused by rapid industrialization. Photocatalytic technology has attracted significant attention because of its ability to utilize solar energy to degrade pollutants, with semiconductor photocatalytic materials being a major research focus. Since Fujishima and Honda's seminal observation of the photocatalytic water-splitting on TiO_2 single-crystal electrodes in 1972[1], substantial advances have been made in the study of photocatalytic materials. Although traditional photocatalytic materials such as TiO_2 exhibit excellent chemical stability and environmental compatibility, the wide bandgap (~3.2 eV) limits light absorption to the ultraviolet range, greatly reducing solar energy utilization efficiency.

To broaden the light-responsive range of photocatalytic materials, researchers have developed various novel semiconductors. Among these, graphitic carbon nitride (g-C_3N_4) has emerged as a particularly promising visible-light-responsive photocatalyst due to its moderate bandgap (~2.7 eV), strong visible-light absorption, and environmental compatibility [2]. In 1996, Teter et al. used density functional theory (DFT) to calculate the energy levels of five carbon nitride (C_3N_4) phases, including the α-phase, β-phase, cubic phase, pseudo-cubic phase, and graphitic phase. The results showed that g-C_3N_4 has the lowest energy state and a layered stacking structure similar to graphene, with adjacent layers held together by weak van der Waals forces [3]. Owing to this unique layered structure, ultrathin g-C_3N_4 nanosheets can be prepared by physical exfoliation. Additional theoretical studies have shown that corrugated, non-planar g-C_3N_4 structures are more thermodynamically stable than planar configurations, a critical factor for practical applications [4]. At the microscopic scale, g-C_3N_4 primarily consists of two structural units: heptazine rings (C_6N_7) [5] and triazine rings (C_3N_3). Nevertheless, pristine g-C_3N_4 still suffers from limitations that significantly hinder its practical performance, including low specific surface area, rapid recombination of photogenerated charge carriers, and insufficient visible-light absorption efficiency.

To address these challenges, various modification strategies have been proposed. Metal doping ions can serve as trapping sites for photogenerated electrons and holes, thereby enhancing interfacial charge transfer efficiency. Nguyen et al. successfully synthesized Fe-doped two-dimensional g-C_3N_4[6]. During photocatalytic reactions, light irradiation excites g-C_3N_4, generating electron-hole pairs. Charge transfer between Fe^{2+}/Fe^{3+} within the g-C_3N_4 lattice effectively suppresses charge recombination, significantly improving electron-hole pair separation efficiency. At an Fe doping concentration of 7%, rhodamine B

(RhB) was nearly completely degraded within 30 min. Using an acid-etching-calcination coupling method, Yang et al. prepared Co-doped two-dimensional g-C_3N_4, achieving a methylene blue degradation efficiency 1.2 times higher than that of bulk g-C_3N_4[7]. Co-doping modified the g-C_3N_4 lattice structure by the formation of Co-N bonds, which simultaneously expanded the visible-light absorption range and accelerated charge transfer, thereby enhancing photocatalytic performance.

A heterojunction is the interfacial region formed when two distinct semiconductors come into contact. Heterojunction formation typically requires the two semiconductors to have similar crystal structures, comparable atomic spacing, and matching thermal expansion coefficients. Common fabrication techniques include vacuum deposition, epitaxial growth, and interfacial alloying. The primary objectives of constructing g-C_3N_4-based heterojunctions are to enhance charge-carrier separation efficiency, shorten charge-transfer distances, and extend the visible-light absorption range, thereby improving photocatalytic degradation performance [8]. Among various configurations, Type II, Z-scheme, and S-scheme heterojunctions are the most prevalent. Sun et al. fabricated a 2D g-C_3N_4/3D ZnO Type II heterojunction, achieving 96.91% sulfamethoxazole (SMZ) degradation after 80 min, a 60.1% enhancement compared to pure 2D g-C_3N_4[9]. To address the challenges of rapid charge recombination and difficult recovery of powdered g-C_3N_4, Feng et al. developed both TiO_2/g-C_3N_4 powder suspensions and immobilized TiO_2/g-C_3N_4 cement pastes through urea and P25 TiO_2 pyrolysis combined with spray-coating [10]. The TiO_2/g- C_3N_4 composite demonstrated significantly improved photocatalytic performance, degrading approximately 98% of RhB and methylene blue within 60 min, owing to its reduced charge recombination rate and extended light absorption range of TiO_2/g-C_3N_4.

Among various modification approaches, transition metal oxides have shown unique advantages in photocatalysis due to their multiple valence states and exceptional catalytic properties. Manganese oxides (MnO_x), representative transition metal oxides, are characterized by high catalytic activity, low cost, and environmental benignity. Combining MnO_x with g-C_3N_4 not only broadens the light-responsive range but also suppresses charge recombination by enhancing interfacial charge transfer mediated by their multivalent states (Mn^{2+}/Mn^{3+}/Mn^{4+}). Moreover, incorporating MnO_x significantly improves the material's adsorption capacity for organic pollutants, further boosting degradation efficiency [11]. Currently, MnO_x/g-C_3N_4 composites are primarily synthesized via hydrothermal and co-precipitation methods, with the latter being more advantageous for practical applications owing to its operational simplicity and mild reaction conditions [12-14]. Nevertheless, most existing studies focus on powder-phase MnO_x/g-C_3N_4 systems, and research on their immobilization onto pervious concrete) for practical

wastewater treatment remains limited.

In this study, g-C_3N_4 was synthesized via thermal polycondensation and subsequently modified with MnO_x through a co-precipitation approach. This approach is expected to leverage the multivalent states of manganese to facilitate interfacial charge transfer and enhance the photocatalytic degradation of pollutants. We systematically investigate the synergistic effect between MnO_x and g-C_3N_4 on the structural, optical, and photochemical properties of the composite. Furthermore, we immobilized the optimized composite on pervious concrete to evaluate its practical applicability in the visible-light-driven degradation of organic pollutants, aiming to provide both mechanistic insights and a potential technological strategy for urban runoff remediation.

2 Materials and Methods

2.1 Materials

All chemical reagents used in this study were analytical grade and used without further purification. Melamine ($C_3H_6N_6$), manganese acetate tetrahydrate (Mn $(CH_3COO)_2 \cdot 4H_2O$), aqueous ammonia (25 wt%), and RhB ($C_{28}H_{31}ClN_2O_3$) were purchased from Tianjin Damao Chemical Reagent Factory. Potassium permanganate ($KMnO_4$) was obtained from Shanghai Shangqiu Weikang Medical Supplies Co., Ltd. Hydrochloric acid (36 wt%) was supplied by Shenyang Pai'er Fine Chemical Products Factory, and absolute ethanol (C_2H_5OH, ≥99.7%) was obtained from Tianjin Fuyu Fine Chemical Co., Ltd.

2.2 Photocatalyst Sample Preparation

2.2.1 Preparation of g-C_3N_4

A certain amount of melamine was placed in a lidded crucible and heated in a muffle furnace. The melamine was calcined at 550°C, 600°C, 650°C, 700°C, and 750°C for 2 h at each temperature under static air, with a heating rate of 5°C·min^{-1}. After being cooled naturally to ambient temperature (25±2°C), the yellow-colored products were harvested and ground into fine powders with an agate mortar. The synthesized materials were denoted as GCN_{550}, GCN_{600}, GCN_{650}, GCN_{700}, and GCN_{750}, corresponding to their respective calcination temperatures. A schematic of the synthesis procedure is shown in Fig. 1. Notably, the precursor was completely volatilized at 750 °C and no solid sample was obtained. Consequently, only the samples calcined at 550-700°C were adopted for the subsequent characterizations and photocatalytic experiments.

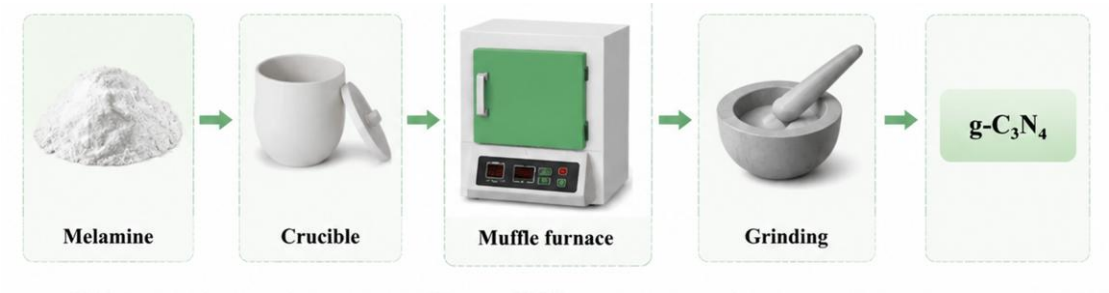


Fig. 1 Preparation process of g-C_3N_4

2.2.2 Preparation of MnO_x/g-C_3N_4

The MnO_x-modified g-C_3N_4 composites were synthesized via a controlled co-precipitation method. Initially, predetermined amounts of g-C_3N_4 (designated as GCN_x, where x = 550-700℃, corresponding to the precursor calcination temperature) were dispersed in deionized water with stoichiometric amounts of $KMnO_4$ and subjected to ultrasonication for 30 min. Simultaneously, manganese acetate solutions (designated as $Mn(OAc)_2$) were prepared at three molar ratios relative to $KMnO_4$ (y = $KMnO_4$: Mn $(OAc)_2$ = 1:2, 3:2, and 2:1). These solutions were then gradually introduced into the ultrasonicated mixture, followed by magnetic stirring at 80°C for 1 h. The resulting suspension was centrifuged and repeatedly washed with deionized water until the pH of the supernatant reached 7. After drying at 80°C for 12 h in a forced-air oven, the products were mechanically ground using an agate mortar to obtain fine powders, which were labeled as Mn-GCN_{x-y} (where x indicates calcination temperature and y specifies the $KMnO_4$: Mn $(OAc)_2$). The synthesis procedure is schematically illustrated in Fig. 2.

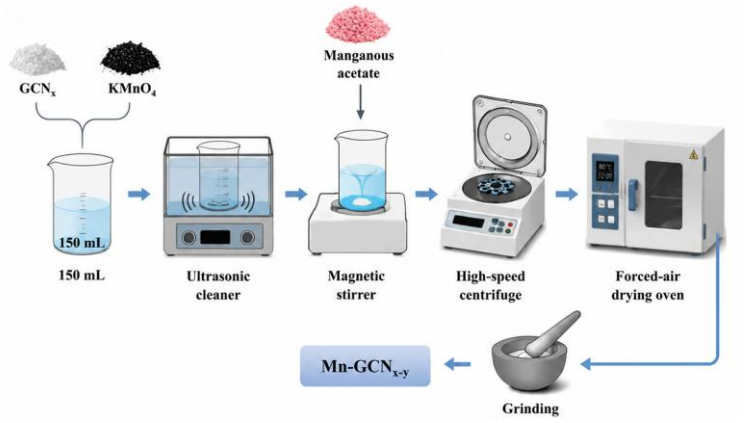


Fig. 2 Preparation process of Mn-GCN_{x-y}

2.2.3 Preparation of Photocatalytic Pervious Concrete

GCN and Mn-GCN coatings were deposited onto concrete surfaces via spraying method with a spray dosage of 0.5 L/m^2 and coating concentrations of 5 g/L. The resulting photocatalytic pervious concrete samples were designated as GPC and MnPC.

2.3 Photocatalyst characterization

Scanning electron microscopy (SEM, Hitachi S4800, Japan) was employed to characterize the morphology and particle size of the as-prepared samples. A transmission electron microscope (TEM) on the JEM-2100F instrument was used to observe the material's microstructure more clearly. X-ray diffraction (XRD) was performed on a Bruker D8 ADVANCE using Cu Kα radiation at a scan rate of 5°/min over the range 10°-80°. The recorded patterns were compared with reference patterns. X-ray photoelectron spectroscopy (XPS) was performed on a Thermo Fisher ESCALAB 250Xi to confirm the chemical composition and oxidation states of the materials. XPS binding energy values were referenced to the carbon peak. Fourier Transform Infrared Spectroscopy (FTIR) was performed using a Thermo Fisher Nicolet 6700 with a KBr beam splitter over the range 4000 cm-1 to 400 cm-1. The UV-Visible Diffuse Reflectance Spectra (UV-DRS) were measured with $BaSO_4$ as the background material (Shimadzu UV2600). A Fluorolog (Edinburgh FLS1000) spectrometer was used to obtain photoluminescence (PL) spectra. A 300 W Xe lamp was used as the light source for photocatalytic degradation.

2.4 Photocatalytic measurements

The synthesized materials were dispersed in 200 mL of a 20 mg/L RhB solution to evaluate their photocatalytic performance. After 30 min of magnetic stirring in the dark to reach adsorption-desorption equilibrium, the suspension was irradiated with visible light from a 300 W xenon lamp for 120 min. Samples were collected at 30 min intervals for analysis, and the degradation efficiency was calculated using Equation (1).

$$D\% = [1 - (C_t/C_0)] \times 100\% \quad (1)$$

where C_t and C_0 are the concentrations of the RhB solution at time t and initially, respectively.

3 Results and discussion

3.1 Characterization of samples

The XRD patterns of the GCN_{700} and Mn-$GCN_{x\text{-}3:2}$ composites are shown in Fig. 3a. GCN_{700} exhibits characteristic diffraction peaks at approximately 2θ=13.0° and 27.3°, while Mn-$GCN_{x\text{-}3:2}$ displays corresponding peaks at 2θ=12.7° and 27.8°, consistent with the typical graphite-like hexagonal phase of g-C_3N_4 (JCPDS 87-1526) [15]. The relatively weak diffraction peaks at 2θ=13.0° for GCN_{700} and the diffraction signal at 2θ=12.7° for Mn-$GCN_{x\text{-}3:2}$ are assigned to the (100) crystal plane of g-C_3N_4. This peak corresponds to the in-plane structural repeating units of conjugated layers and reflects the macrocyclic structure between tri-s-triazine units. The shifted diffraction peaks at 2θ = 12.7 ° and 27.8°

for Mn-$GCN_{x\text{-}3:2}$ composites reveal changes in interlayer spacing. Such variation is probably caused by the interaction between Mn d-orbital and π-system of g-C_3N_4. Additionally, Mn-$GCN_{x\text{-}3:2}$ exhibits characteristic diffraction peaks of at 2θ = 37.1°, 42.6°, 57.7°, and 66.8°, which are assigned to the (111), (102), (110), and (301) crystal planes, respectively [16]. Their broad forms and weak intensities indicate low MnO_x content or poor crystallinity.

The full-survey XPS spectra in Fig. 3b confirm the existence of C, N, Mn and O elements in GCN_{700} and Mn-$GCN_{x\text{-}3:2}$. All spectra were charge-calibrated using the C 1s peak at 284.8 eV as the reference, and the corresponding deconvolution results are presented in Fig. 3c. The C 1s spectrum of GCN_{700} can be split into two peaks: the C-C signal at 284.6 eV originating from surface adventitious carbon, and the characteristic peak of sp^2-hybridized N=C-N (288.2 eV) within g-C_3N_4 skeleton. For Mn-$GCN_{x\text{-}3:2}$, the C 1s spectrum exhibits three peaks at C-C (284.6 eV), C-O (286.1 eV), and N=C-N (288.2 eV). The newly-appeared C-O bond verifies the formation of interfacial Mn-O-C linkage between MnO_x and g-C_3N_4. As shown in Fig. 3d, the N 1s spectra of both GCN_{700} and Mn-$GCN_{x\text{-}3:2}$ are deconvoluted into four peaks, which are assigned to sp^2-hybridized N in C=N-C (398.5 eV), sp^2-hybridized bridging N in C-N (400.1 eV), sp^3-hybridized terminal N-H (401.2 eV), and charge effects from π-excitation (404.1 eV), respectively [17].

The Mn 2p spectrum of Mn-$GCN_{x\text{-}3:2}$ were shown in Fig. 3e, which display distinct spin-orbit doublets located at 642.1 eV (Mn $2p_{3/2}$) and 653.8 eV (Mn $2p_{1/2}$). Peak deconvolution of the Mn $2p_{3/2}$ spectrum verifies the presence of Mn^{2+}, Mn^{3+}, and Mn^{4+} for Mn-$GCN_{550\text{-}3:2}$ and Mn-$GCN_{600\text{-}3:2}$. By comparison, Mn-$GCN_{650\text{-}3:2}$ and Mn-$GCN_{700\text{-}3:2}$ fabricated at elevated temperatures only contain Mn^{3+} and Mn^{4+}[18-19], with no detectable Mn^{2+} species. Systematic analysis reveals that increasing the calcination temperature eliminates the Mn^{2+} phase entirely. Meanwhile, the relative proportion of Mn^{3+} increases monotonically, whereas the fraction of Mn^{4+} decreases gradually. Specifically, quantitative XPS analysis of Mn-$GCN_{700\text{-}3:2}$ reveals that the Mn^{3+} species predominates with a relative content of approximately 70%, significantly exceeding the Mn^{4+} fraction of 30%. Mn-$GCN_{700\text{-}3:2}$ exhibits the highest Mn^{3+} and lowest Mn^{4+} concentrations. Notably, the Mn $2p_{3/2}$ peak in Mn-$GCN_{700\text{-}3:2}$ shows a slight shift toward higher binding energy compared to other samples, attributed to changes in the electron cloud density around Mn atoms, which affect the core-level binding energy [20]. Given that Mn^{3+} possesses a lower electron density compared to Mn^{4+}, its high prevalence reduces the shielding effect on the Mn 2p electrons, thereby accounting for the observed increase in binding energy.

Fig. 3f shows the O 1s spectrum, which displays two peaks at 529.9 eV and 531.6 eV, corresponding to lattice oxygen (O_{latt}) and adsorbed oxygen (O_{ads}) species [21]. These oxygen species play distinct roles in photocatalytic reactions, where their relative concentrations and chemical environments may influence surface active sites and reaction kinetics. Meanwhile, the relative content of O_{ads} content increases from 35.26% to 47.67% as temperature increases, accompanied by a decline in O_{latt}. The maximal O_{ads} content achieved in Mn-$GCN_{700\text{-}3:2}$ is beneficial for trapping photogenerated charge carriers and accelerating the generation of reactive oxygen species during the photocatalytic degradation process. The synergistic contributions from dominant Mn^{3+} phase and abundant O_{ads} jointly endow Mn-$GCN_{700\text{-}3:2}$ with outstanding photocatalytic performance of RhB [22].

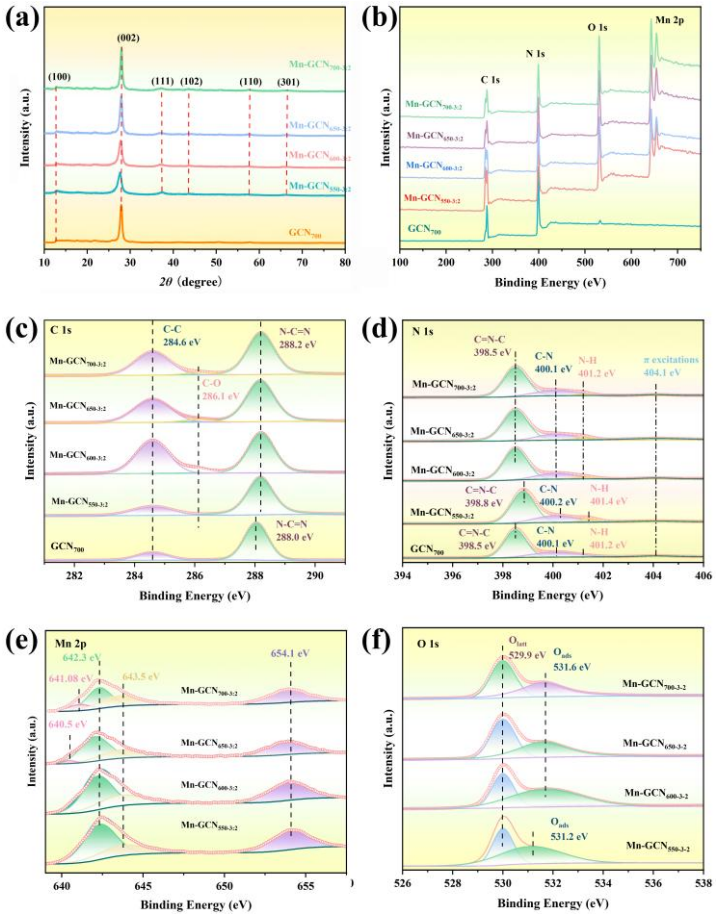


Fig. 3 (a) XRD patterns of GCN_{700} and Mn-$GCN_{x\text{-}3:2}$; (b) XPS survey spectra of GCN_{700} and Mn-$GCN_{x\text{-}3:2}$; (c-f) XPS patterns of GCN_{700} and Mn-$GCN_{x\text{-}3:2}$

The surface morphologies of GCN_{700} and Mn-$GCN_{x\text{-}3:2}$ were characterized by SEM, as shown in Fig. 4a-e. Mn-$GCN_{550\text{-}3:2}$ displays a composite microstructure consisting of irregular bulk agglomerates decorated with MnO_x nanoparticles, as verified by XRD for the formation of multilayer g-C_3N_4 via thermal polycondensation of melamine. With increasing calcination temperature, the bulk architecture of Mn-$GCN_{600\text{-}3:2}$ initially loosens due to the gradual thermal exfoliation of stacked g-C_3N_4 layers. Further

increasing the temperature to 650 °C induces prominent particle refinement and enlarged interlayer spacing in Mn-$GCN_{650\text{-}3:2}$. Notably, the Mn-$GCN_{700\text{-}3:2}$ sample achieves optimized structural dispersion with negligible particle agglomeration. In contrast, Mn-$GCN_{700\text{-}3:2}$ is decorated with uniform spherical MnO_x nanoparticles that possess narrow particle size distribution and rough surface texture, which are unambiguously identified as MnO_x species by synergistic XRD and XPS analyses.

The TEM image of Mn-$GCN_{700\text{-}3:2}$ is shown in Fig. 4f. The substance exhibits reveals a graphite-like layered structure with slightly curled edges. This structural characteristic is confirmed by complementary XRD and XPS investigations. Lattice spacings of 0.34±0.01 nm and 0.23±0.01 nm are indexed to the (111) plane of MnO_2 and the (002) plane of g-C_3N_4, respectively, consistent with XRD estimates [23-24]. Dark-contrast regions likely correspond to MnO_2 nanoparticles, further supported by XRD and XPS.

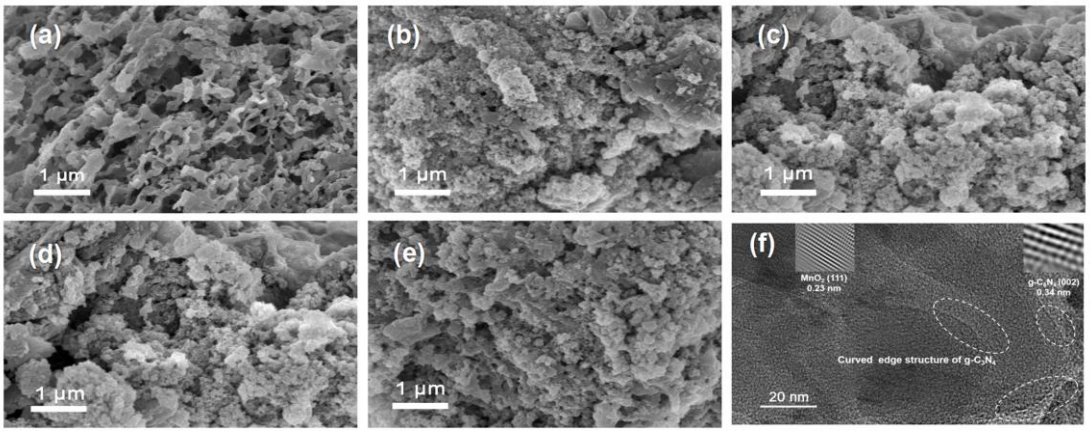


Fig. 4 (a-e) SEM images of GCN_{700}, Mn-$GCN_{X\text{-}3:2}$; (f) TEM images of Mn-$GCN_{700\text{-}3:2}$: (g-j) elemental mapping images of C, N, O, and Mn in Mn-$GCN_{700\text{-}3:2}$

The particle size distribution of all samples was statistically analyzed, and the corresponding results are illustrated in Fig. 5a-e. GCN_{700} exhibits a unimodal distribution spanning 0.10-0.60 μm, with a pronounced peak at 0.20-0.30 μm and a mean particle size of 0.36 μm. The particle size of the Mn-$GCN_{x\text{-}3:2}$ composites gradually decreases with increasing calcination temperature. The average particle size of Mn-$GCN_{550\text{-}3:2}$ is 0.08 μm, with a distribution peak between 0.03 and 0.07 μm. Mn-$GCN_{600\text{-}3:2}$ has a smaller average size of 0.06 μm but shows a similar distribution profile.

Benefiting from the high-temperature thermal refinement effect, Mn-$GCN_{650\text{-}3:2}$ displays a further reduced particle size, with the distribution peak shifting to 0.03-0.04 μm and an average diameter of 0.04 μm. Mn-$GCN_{700\text{-}3:2}$ exhibits the most optimal particle refinement, delivering a narrow and concentrated size distribution centered at 0.01-0.02 μm and a minimum average particle size of 0.02 μm, which is

nearly one order of magnitude smaller than that of pure GCN_{700}. Such ultra-fine, uniformly dispersed nanoparticles and expanded interlayer structure are conducive to exposing more active sites and accelerating interfacial charge transfer, thereby endowing the composite with superior catalytic performance.

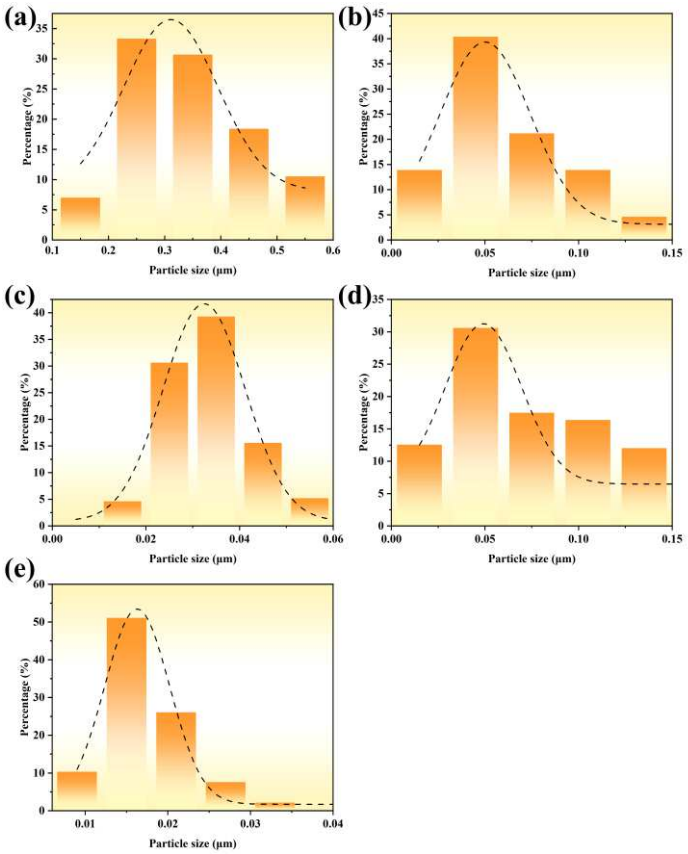


Fig. 5 (a-e) Particle size of GCN_{700}, Mn-$GCN_{550\text{-}3:2}$, Mn-$GCN_{600\text{-}3:2}$; Mn-$GCN_{650\text{-}3:2}$, and Mn-$GCN_{700\text{-}3:2}$

The FT-IR spectra of Mn-$GCN_{700\text{-}3:2}$ and GCN_{700} are shown in Fig. 6a. The two samples share nearly identical characteristic fingerprint peaks, demonstrating that the intrinsic framework of g-C_3N_4 is well preserved after MnO_x modification. Theabsorption bands located at 1206.57 cm^{-1} and 1637.91 cm^{-1} are assigned to the asymmetric C-N and symmetric C=N stretching vibrations, respectively [23]. A broad absorption band ranging from 3081.87 cm^{-1} to 3418.72 cm^{-1} originates from the stretching vibrations of the -NH_2, -NH, and -OH groups, confirming the preservation of amino functional groups derived from the thermal polycondensation of melamine. The sharp characteristic peak at 810.15 cm^{-1} for Mn-$GCN_{700\text{-}3:2}$ is assigned to the typical stretching vibration of 3-s-triazine heterocycles in g-C_3N_4. This observation further verifies that the introduction of MnO_x hardly alters the fundamental crystal backbone of the g-C_3N_4, which is highly consistent with our previous XRD results. Compared to GCN_{700} (807.23 cm^{-1}), a slight blue-shift accompanied by enhanced peak intensity at the triazine-related vibration band is

observed for Mn-$GCN_{700\text{-}3:2}$. This phenomenon strongly implies the occurrence of electronic cloud redistribution at the MnO_x/g-C_3N_4 hetero-interface, which may be triggered by local lattice polarization and interfacial electronic interaction [25].

Optical-absorption properties of GCN_{700} and Mn-$GCN_{700\text{-}3:2}$ were investigated via UV-DRS as presented in Fig. 6b. Distinctly, Mn-$GCN_{700\text{-}3:2}$ delivers remarkably strengthened visible-light absorption capacity in the region of 400-800 nm, in sharp contrast with the limited visible-light harvesting of pristine GCN_{700}. The broad absorption tail extending to the long-wavelength visible-light region indicates that MnO_x incorporation effectively broadens the spectral-response window of the composite, enabling the utilization of low-energy visible-light photons. The optical band gaps of the prepared samples were estimated using the Kubelka-Munk function [26], with the specific calculation Equation as follows [27]:

$$(\alpha h\nu)^n = K(h\nu - E_g) \quad (2)$$

where α, ν, h, K, and E_g are absorbance, photon frequency, Planck's constant, proportionality constant, and band-gap energy, respectively. The Tauc plot was obtained by plotting hν versus (αhν) n, with n=2 for g-C_3N_4, an indirect semiconductor.

As shown in Fig. 6c, Tauc plot analysis indicates that GCN_{700} exhibits an optical band gap of 2.95 eV, which is slightly larger than the commonly reported theoretical value (~2.7 eV) of bulk g-C_3N_4 and matches well with previous literature reports [28-30]. Such band-gap widening can be attributed to the high-temperature calcination-induced structural optimization at 700°C, improved crystallinity, well-ordered interlayer stacking and decreased intrinsic defect density collectively reconstruct the electronic band structure [31]. Applications of GCN_{700} in solar-driven photocatalytic reactions are theoretically supported by its band-gap characteristics, which indicate that its principal light-absorption range lies in the ultraviolet and partial visible regions (λ<420 nm). The band gap of Mn-$GCN_{700\text{-}3:2}$ is 1.76 eV, which is 1.19 eV lower than that of GCN_{700}. The observed red shift is consistent with this significant band-gap narrowing, which broadens the light-absorption range of Mn-$GCN_{700\text{-}3:2}$, reduces the energy required for charge-carrier excitation, and enhances material conductivity and carrier mobility. The results demonstrate that incorporating MnO_x improves the optical characteristics of the composite material.

The recombination behaviors of photogenerated electron-hole pairs can be indirectly measured by PL spectroscopy. Generally, lower PL emission intensity corresponds to suppressed radiative recombination and higher charge-separation efficiency, thus generating more available charge carriers to participate in surface redox reactions [32]. As displayed in Fig. 6d, GCN_{700} exhibits a distinct photoluminescence emission peak centered at 480 nm, which falls within the typical the characteristic

emission region (450-500 nm) of graphitic carbon nitride. The restricted photocatalytic activity of GCN_{700} is attributed to rapid recombination of photogenerated electron-hole pairs, as indicated by its relatively high photoluminescence intensity. By contrast, obvious quenched photoluminescence is detected in Mn-$GCN_{700\text{-}3:2}$, demonstrating that MnO_x/g-C_3N_4 heterostructure significantly inhibits the recombination of photoinduced electron-hole pairs and accelerates spatial charge separation. Benefiting from the built-in hetero-interface, rapid interfacial charge migration pathways are established to prolong the lifetime of active charge carriers. Importantly, the conclusions drawn from PL spectra are in agreement with the above-mentioned optical-absorption results from UV-vis DRS, providing consistent evidence for the optimized electronic properties of Mn-$GCN_{700\text{-}3:2}$ composite.

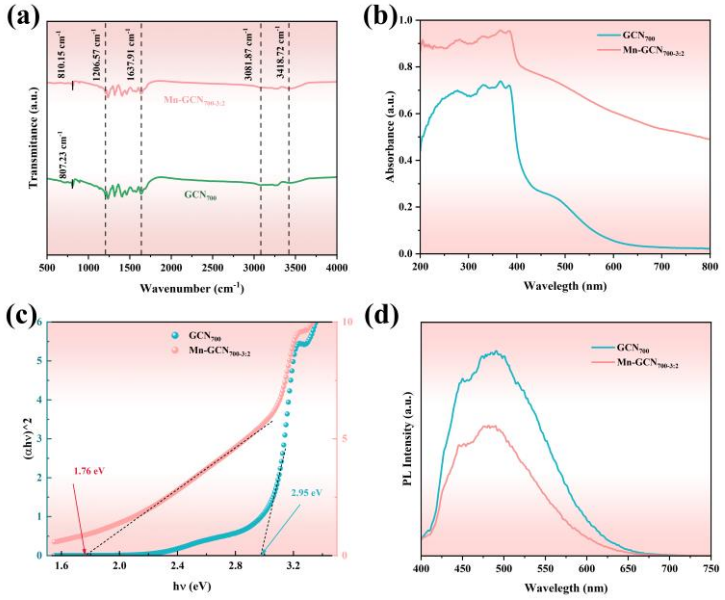


Fig. 6 (a) FT-IR patterns; (b) UV-vis DRS spectra; (c) Band Gap Diagrams; (d) PL spectra of GCN_{700}, Mn-$GCN_{700\text{-}3:2}$

3.2 Photocatalytic degradation of RhB for GCN_x

The photocatalytic degradation of RhB by GCN_x (x=550-700 °C) was investigated under Xe lamp irradiation. With the elevation of calcination temperature, the product yield of GCN_x gradually decreased, which originated from the continuous deammoniation polycondensation and thermal bond cleavage of melamine-derived g-C_3N_4 . Severe thermal decomposition ultimately led to complete volatilization of the g-C_3N_4 framework at 750℃ [33].

The pH-dependent photocatalytic degradation performance of RhB for GCN_x is displayed in Fig.7. GCN_x present significantly enhanced degradation performance under acidic conditions (pH=3), which is consistent with other reports [34]. Under visible-light irradiation for 120 min with a catalyst dosage of 0.01 g, the photocatalytic degradation of RhB for GCN_{700} is increased by 38.36% compared with that of

GCN_{550}, demonstrated that high-temperature calcination effectively optimizes the photocatalytic reactivity of g-C_3N_4. The pH-dependent photocatalytic degradation performance of RhB for GCN_{700} is shown in Fig. 8a. With the catalyst dosage of 0.01 g, the degradation efficiencies reached reached 75.57% (pH=3), 59.87% (pH=5), 26.41% (pH=7), and nearly negligible activity at pH=9. The distinct pH selectivity is dominated by the electrostatic interaction between the catalyst surface and RhB molecules. Given the pKa value of RhB (~4.4), RhB exists mainly in cationic form at pH<4.0, which can be strongly adsorbed on the negatively charged g-C_3N_4. surface via electrostatic attraction. In contrast, zwitterionic RhB generated at pH>4.0 induces interfacial Coulomb repulsion, severely restricting molecular adsorption and interfacial redox reaction. Therefore, acidic conditions are thermodynamically favorable for RhB photodegradation.

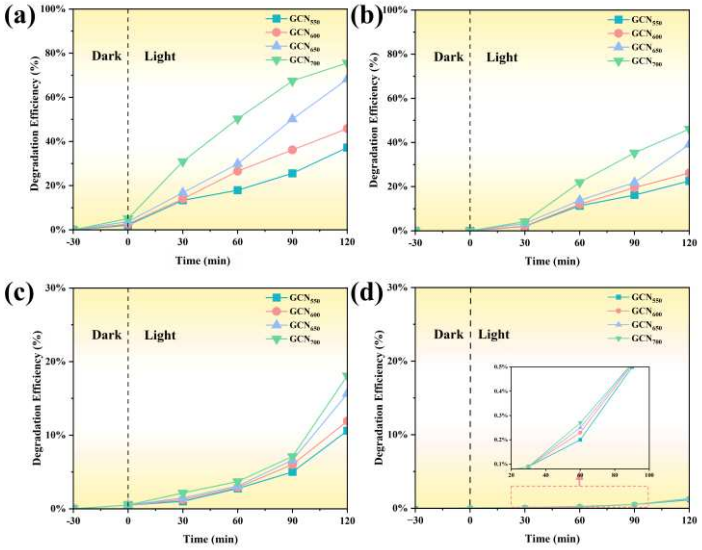


Fig. 7 Photocatalytic degradation performance of RhB for GCN_x under visible-light irradiation at different pH values: (a) pH=3, (b) pH=5, (c)pH=7 and (d)pH=9

The pH-dependent photocatalytic degradation performance of RhB for Mn-GCN_x is displayed in Fig.8a, which present best degradation performance under acidic conditions (pH=3). The catalyst dosage effect on RhB degradation was investigated at pH = 3 and shown in Fig.8b. The optimal dosage is determined to be 0.06 g, achieving a superior degradation efficiency of 99.75% within 90 min, which is 49.43% higher than that of 0.01 g dosage. The moderate catalyst loading provides abundant exposed active sites, promotes interfacial charge transfer, and optimizes light propagation and mass transfer efficiency. Nevertheless, excessive catalyst dosage (0.12 g) causes severe particle aggregation, which induces light shielding effect, blocks active sites, increases light scattering, and weakens charge-mass transfer dynamics, thus reducing the degradation efficiency to 89.75%.

As illustrated in Fig. 8c, GCN_{700} maintains a high degradation efficiency of 87.43% after six consecutive cycling tests, verifying its excellent structural and photochemical stability under 60 min visible-light irradiation at pH 3 with 0.06 g catalyst loading. The cycling performance of GCN_{700} has great potential for sustainable photocatalytic wastewater treatment.

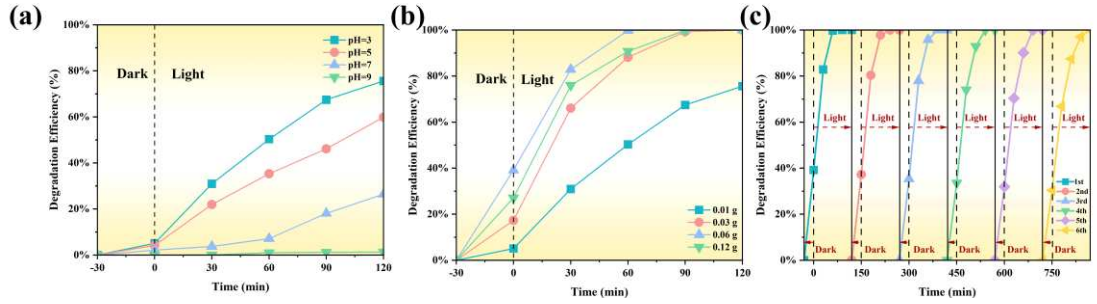


Fig. 8 (a-b) photocatalytic degradation performance of GCN_{700} towards RhB at different pH values and dosages; (c) cycling performance of GCN_{700} in photocatalytic degradation of RhB

3.3 Photocatalytic degradation of RhB for MnO_x/g-C_3N_4

The photocatalytic degradation performance of RhB for Mn-GCN_{x-y} is presented in Fig. 9a-c. Consistent with GCN_x, all Mn-GCN composites achieve optimal photocatalytic activity under acidic conditions (pH=3). After 90 min visible-light irradiation, the degradation efficiencies of RhB for Mn-$GCN_{550\text{-}3:2}$, Mn-$GCN_{600\text{-}3:2}$, and Mn-$GCN_{650\text{-}3:2}$ were of 92.35%, 98.96%, and 99.45%, respectively. Notably, Mn-$GCN_{700\text{-}3:2}$ realizes nearly complete RhB removal, exhibiting a prominent temperature-dependent positive correlation between calcination temperature and photocatalytic performance. Benefiting from the optimized microstructure, narrowed band gap, and highly efficient charge separation confirmed by SEM, UV-vis DRS and PL spectra, Mn-GCN_{700} series composites show consistently superior activity compared with low-temperature counterparts. Specifically, Mn-$GCN_{700\text{-}3:2}$ achieves over 97% RhB degradation within only 60 min, which is 49.51% higher than pristine GCN_{700}. The precursor molar ratio of $KMnO_4$/Mn $(OAc)_2$ was further optimized to construct the optimal MnO_x/g-C_3N_4 heterostructure (Fig. 9d). At a fixed calcination temperature of 700 ºC and catalyst dosage of 0.01 g, the 3:2 molar ratio is verified as the optimal proportion. Such outstanding performance originates from the balanced generation of active MnO_x species and the strongest interfacial electronic interaction between MnO_x and g-C_3N_4 matrix, which effectively accelerates charge migration and suppresses photogenerated carrier recombination. Consequently, Mn-$GCN_{700\text{-}3:2}$ with the optimal precursor ratio was selected for subsequent mechanism exploration.The catalyst dosage was subsequently optimized for Mn-$GCN_{700\text{-}3:2}$ under pH=3. As displayed in Fig. 9e, the 0.06 g dosage enables an ultra-high RhB degradation efficiency of 99.81% within 30 min, achieving complete pollutant elimination after 60 min irradiation.This non-

monotonic relationship between dosage and activity stems from particle agglomeration at higher loadings. Agglomeration decreases solution transmittance and light utilization efficiency by creating optical shielding that limits both photon penetration and active-site accessibility [34].

The cycling stability of Mn-GCN$_{700\text{-}3:2}$ and was evaluated via six repeated photodegradation experiments and shown in Fig. 9f. Mn-GCN$_{700\text{-}3:2}$ exhibited excellent cycling stability, retaining 90.13% degradation efficiency after six consecutive cycles, which is 2.7% higher than pristine GCN$_{700}$. The significantly improved stability and photocatalytic performance are attributed to the synergistic effect between uniformly dispersed MnO_x nanoparticles and the g-C_3N_4. The constructed heterojunction effectively inhibits photogenerated charge recombination, promotes interfacial electron transfer, and prevents photocorrosion during long-term cycling. The above results demonstrate that the rational regulation of calcination temperature and precursor ratio is an effective strategy to fabricate high-efficiency and stable g-C_3N_4-based composite photocatalysts for environmental remediation.

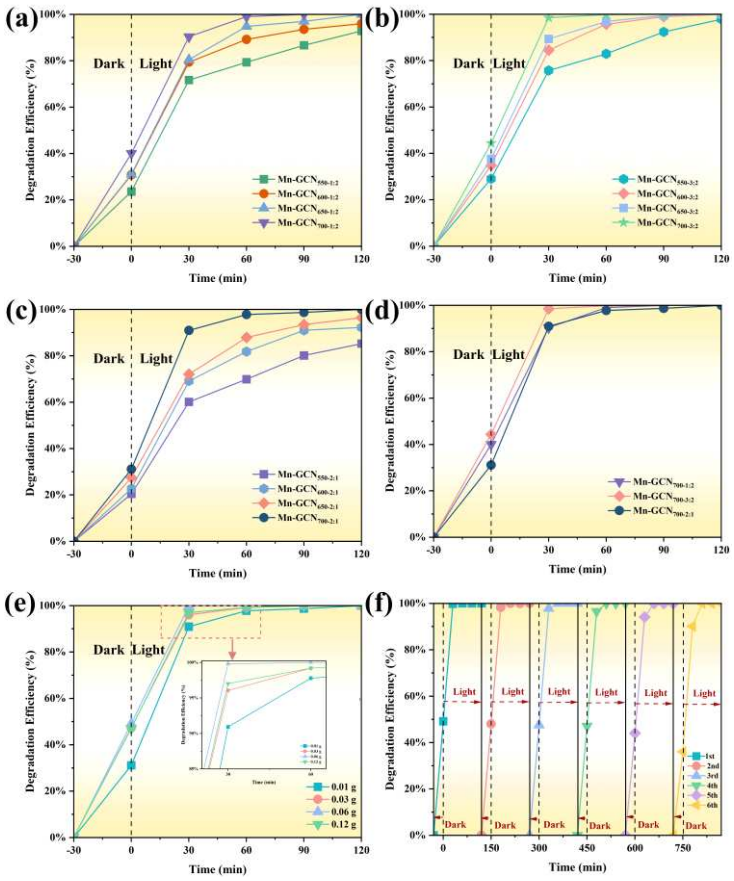


Fig.9 (a-d) photocatalytic degradation performance of RhB for Mn-GCN$_{x\text{-}1:2}$ (a), Mn-GCN$_{x\text{-}3:2}$ (b), Mn-GCN$_{x\text{-}2:1}$ (c), and Mn-GCN$_{700\text{-}y}$ (d). (e) photocatalytic degradation performance of RhB for different dosages of Mn-GCN$_{700\text{-}3:2}$. (f) cycling performance for Mn-GCN$_{700\text{-}3:2}$

3.4 Photocatalytic mechanism

The FT-IR spectra indicate that the introduction of Mn does not destroy the fundamental framework of GCN_{700}, but the slight shifts in characteristic peaks suggest strong interfacial interactions between MnO_x and g-C_3N_4. UV-vis DRS and the corresponding Tauc plots demonstrate that compared to pristine GCN_{700}, Mn-$GCN_{700\text{-}3:2}$ exhibits a significantly narrowed band gap and enhanced visible-light absorption. This broadened photo-response enables more efficient generation of photogenerated carriers under visible light irradiation.

However, the overall photocatalytic efficiency is also governed by the separation efficiency of the carriers. The PL spectra show a dramatically quenched emission peak for Mn-$GCN_{700\text{-}3:2}$ compared to GCN_{700}, indicating that the introduction of MnO_x effectively suppresses the recombination of photogenerated electron-hole pairs.[35] Mechanistically, this suppression is attributed to the mixed-valence states of Mn^{3+}/Mn^{4+} revealed by XPS, where Mn^{3+} predominates (70%). These Mn species serve as effective electron traps. Under visible light, g-C_3N_4 is excited to generate electrons (e^-) and holes (h^+) [36]. Given the predominant Mn^{3+} species, photogenerated electrons are preferentially captured by Mn^{3+}, reducing it to Mn^{2+} or captured by Mn^{4+} to form Mn^{3+}. The trapped electrons are subsequently transferred to adsorbed O_2 to generate superoxide radicals ($\cdot O_2^-$), while the Mn species return to their higher oxidation states [37]. This establishes a dynamic Mn^{3+}/Mn^{4+} redox cycle, which markedly promotes interfacial charge transfer and mitigates recombination. Meanwhile, the holes (h^+) remaining in the valence band can directly oxidize RhB or react with H_2O/OH^- to produce hydroxyl radicals ($\cdot OH$) [37-38]. Ultimately, RhB is degraded and inorganic ions through the synergistic action of $\cdot O_2^-$, $\cdot OH$, and h^+.

The deduced mechanism can be summarized by the following equations:

$$Mn^{3+} + e^- \rightarrow Mn^{2+} \quad (3)$$

$$Mn^{4+} + e^- \rightarrow Mn^{3+} \quad (4)$$

$$Mn^{2+} + O_2 \rightarrow Mn^{3+} + \cdot O_2^- \quad (5)$$

$$e^- + O_2 \rightarrow \cdot O_2^- \quad (6)$$

$$h^+ + H_2O/OH^- \rightarrow \cdot OH \quad (7)$$

$$\cdot O_2^- + \cdot OH + h^+ + Rh\,B \rightarrow degradation\ products \quad (8)$$

3.5 Applications of photocatalytic materials

To broaden the practical application of photocatalysts in engineering projects, GCN_{700} and Mn-$GCN_{700\text{-}3:2}$ were sprayed onto pervious concrete surfaces by air-spray technology and designated as GPC and MnPC. As shown in Fig 10, the photocatalytic performance of RhB for GPC and MnPC were 45.59% and 78.11% under visible light within 120 min, respectively. MnPC exhibits superior photocatalytic

activity, and the resultant pervious concrete satisfies the criteria stipulated in *Technical Specification for Pervious Cement Concrete Pavement* (CJJ/T 135-2009). The specification requires that pervious concrete should possess a 28 d porosity ≥ 10%, water permeability coefficient ≥ 0.5 mm/s, compressive strength ≥ 20 MPa, and flexural strength ≥ 2.5 MPa. Furthermore, MnPC modified pervious concrete outperforms conventional pervious concrete in all these performance indicators.

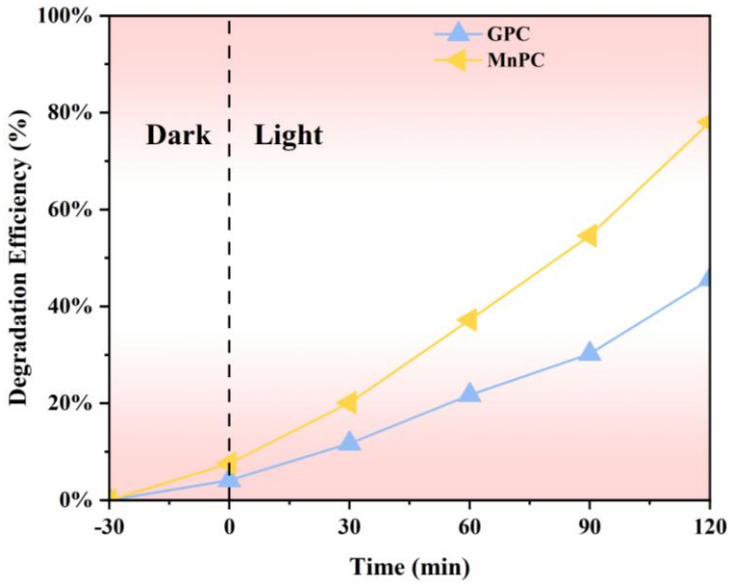


Fig. 10 photocatalytic degradation of RhB for GPC and MnPC

4 Conclusion

MnO_x-modified g-C_3N_4(Mn-GCN) were successfully fabricated onto pervious concrete via a spraying method for visible-light-driven RhB degradation. With the catalysts dosage of 0.01g, the degradation of Rh B for Mn-$GCN_{700\text{-}3:2}$ reached 99.83% at pH of 3 within 60 min under visible-light, which is 49.51% higher than pristine GCN_{700}. Mn-$GCN_{700\text{-}3:2}$ exhibited excellent cycling stability, retaining 90.13% degradation efficiency after six consecutive cycles. XPS analysis revealed that Mn(III) constituted 70% of the Mn species, forming a mixed-valence Mn^{3+}/Mn^{4+} system, while FT-IR confirmed strong interfacial coupling between MnO_x and g-C_3N_4. UV-vis DRS, band-gap, and PL results demonstrated that Mn incorporation markedly narrowed the band gap, enhanced visible-light absorption, and suppressed charge recombination. The $Mn^{3+/}Mn^{4+}$ redox cycle served as electron traps to promote charge separation and O_2 activation into $\cdot O_2^-$, which cooperated with ·OH and h^+ to drive efficient RhB degradation. When applied to pervious concrete at 5 g/L, the system achieved 78.11% RhB degradation within 120 min under visible light, exceeding GPC (32.52%) and meeting the *Technical Specification for Pervious Cement Concrete Pavement*. Although abrasion caused some activity loss, the system

maintained effective photocatalytic performance, demonstrating its potential for sustainable water purification in sponge-city infrastructure. Further optimization of catalyst loading and abrasion resistance is expected to enhance long-term engineering applicability.

Acknowledgments

This work was supported by Liaoning Province Science and Technology Plan Joint Program (Natural Science Foundation-General Project) [2024-MSLH-362], Liaoning Provincial Department of Education (Natural Science Foundation-Youth Project) [LJ212510142043].

CRediT authorship contribution statement

Xuelu Xu: Investigation, Validation, Writing–original draft, Resources. **Yue Dong:** Conceptualization, Methodology, Writing–review & editing. **Sijin Zhang:**Validation, Supervision. **Shuai Yang:**Validation, Supervision. **Jin Meng:** Validation. **Jie Huang:** Validation. **Lili Jiang:** Validation, Supervision.

Data availability

The authors have permission of the data.

References

[1] Fujishima A, Honda K (1972) Electrochemical Photolysis of Water at a Semiconductor Electrode. Nature. 238(5358):37-38. https://doi.org/10.1038/238037a0

[2] Ruan Y, Hu YN, Cheng H (2025) Recent Progress in g-C_3N_4-Based Photocatalysts for Organic Pollutant Degradation: Strategies to Improve Photocatalytic Activity, Catalysts. 15(2):148. https://doi.org/10.3390/catal15020148

[3] Teter DM, Hemley RJ (1996) Low-compressibility carbon nitrides, Science. 271(5245):53-55. https://doi.org/10.1126/science.271.5245.53

[4] Jiang JZ, Yu LL, Peng JH, Gong WP, Sun W (2025) Advance in the modification of g-C_3N_4-based composite for photocatalytic H_2 production, Carbon Letters. 35(2):417-440. https://doi.org/10.1007/s42823-024-00853-8

[5] Azofra LM, MacFarlane DR, Sun CH (2016) A DFT study of planar vs. corrugated graphene-like carbon nitride (g-C_3N_4) and its role in the catalytic performance of CO_2 conversion, Physical Chemistry Chemical Physics. 18(27):18507-18514. https://doi.org/10.1039/c6cp02453j

[6] Van MN, Mai OLT, Do CP, Thi HL, Manh CP, Manh HN, Thi DP, Danh BD (2020) Fe-doped g-C_3N_4: High-performance photocatalysts in rhodamine B decomposition, Polymers.12(9):1963. https://doi.org/10.3390/polym12091963

[7] Yang X, Tian Z, Chen YF, Huang H, Hu J, Wen B (2021) In situ synthesis of 2D ultrathin cobalt doped g-C_3N_4 nanosheets enhances photocatalytic performance by accelerating charge transfer, Journal of Alloys and Compounds. 859:157754. https://doi.org/10.1016/j.jallcom.2020.157754

[8] Liang JC, Li XQ, Zuo JL, Lin J, Liu ZL (2021) Hybrid 0D/2D heterostructures: in-situ growth of 0D g-C_3N_4 on 2D BiOI for efficient photocatalyst, Advanced Composites and Hybrid Materials. 4(4):1122-1136. https://doi.org/10.1007/s42114-021-00341-x

[9] Sun Q, Sun Y, Zhou MY, Cheng HM, Chen HY, Dorus B, Lu M, Le T (2022) A 2D/3D g-C_3N_4/ZnO heterojunction enhanced visible-light driven photocatalytic activity for sulfonamides degradation, Ceramics International. 48(5):7283-7290. https://doi.org/10.1016/j.ceramint.2021.11.289

[10] Feng SL, Li F (2021) Photocatalytic dyes degradation on suspended and cement paste immobilized TiO_2/g-C_3N_4 under simulated solar light, Journal of Environmental Chemical Engineering. 9(4):105488. https://doi.org/10.1016/j.jece.2021.105488

[11] Zhang T, Li B, Wang CF, Wu SL, Zhu SL, Jiang H, Zheng YF, Li ZY, Cui ZD, Zhang Y, Chu

PK, Liu XM (2024) Tunning the bandgap of MnO_2 homojunction by building active high-index facet to achieve rapid electron transfer for enhanced photocatalytic sterilization, Journal of Materials Science & Technology. 168:265-275. https://doi.org/10.1016/j.jmst.2023.05.059

[12] Alharthi FA, Hasan I (2024) Screen-printed carbon electrode modified by δ-MnO_2/S@g-C_3N_4 nanocomposite for dopamine sensing using linear sweep voltammetry, Journal of Electronic Materials. 53(4):2124-2134. https://doi.org/10.1007/s11664-024-10924-1

[13] Wen TC, Xiong SL, Zhao HH, Wang JZ, Wang CM, Long ZS, Xiong L, Qian GW (2024) Polylactic acid-based dressing with oxygen generation and enzyme-like activity for accelerating both light-driven biofilm elimination and wound healing, Burns & Trauma. 12:tkae041. https://doi.org/10.1093/burnst/tkae041

[14] Chacko B, Wuppulluri M (2025) A comparative study on the structural, chemical, morphological and electrochemical properties of α-MnO_2, β-MnO_2 and δ-MnO_2 as cathode materials in aqueous zinc-ion batteries, Materials for Renewable and Sustainable Energy.14(1):10. https://doi.org/10.1007/s40243-024-00281-8

[15] Zulfiqar S, Liu S, Rahman N, Tang H, Shah S, Yu XH, Liu QQ (2021) Construction of S-scheme MnO_2@CdS heterojunction with core–shell structure as H_2-production photocatalyst, Rare Metals. 40(9):2381-2391. https://doi.org/10.1007/s12598-020-01616-w

[16] Rivera-Lugo YY, Félix-Navarro RM, Trujillo-Navarrete B, Reynoso-Soto EA, Silva-Carrillo C, Cruz-Gutiérrez CA, uiroga-González QE, Calva-Yáñez JC (2020) Flower-like δ-MnO_2 as cathode material of Li-ion batteries of high charge-discharge rates, Fuel. 287(31):119463. https://doi.org/10.1016/j.fuel.2020.119463

[17] Qiu PX, Chen H, Xu CM, Zhou N, Jiang F, Wang X, Fu YS (2015) Fabrication of an exfoliated graphitic carbon nitride as a highly active visible light photocatalyst, Journal of Materials Chemistry A. 3(48):24237-24244. https://doi.org/10.1039/c5ta08406g

[18] Liu HX, Kong LY, Wang HR, Li JY, Wang JQ, Zhu YF, Li HW, Jian ZC, Jia XB, Su Y, Zhang SL, Mao JF, Chen SQ, Liu Y, Chou SL, Xiao Y (2024) Reviving Sodium Tunnel Oxide Cathodes Based on Structural Modulation and Sodium Compensation Strategy Toward Practical Sodium-Ion Cylindrical Battery, Advanced Materials. 36(41):2407994. https://doi.org/10.1002/adma.202407994

[19] Cestaro R, Rheingans B, Schweizer P, Müller A, Vockenhuber C, Cancellieri C, Jeurgens LPH, Schmutz P (2024) Well-defined synthesis of crystalline MnO, Mn_2O_3, and Mn_3O_4 phases by anodic

electrodeposition and calcination, Journal of the American Ceramic Society. 107(12):8676-8690. https://doi.org/10.1111/jace.20081

[20] Yashas SR, Shivaraju HP, Pema G, Swamy NK, Namratha K, Gurupadayya B, Madhusudan P (2021) Sonochemical synthesis of graphitic carbon nitride-manganese oxide interfaces for enhanced photocatalytic degradation of tetracycline hydrochloride. Environmental Science and Pollution Research. 28(4):4778-4789. https://doi.org/10.1007/s11356-020-10813-0

[21] Christy DE, Vijayakumar E, Bosco AJ, Johnson PM (2023) Dahlia flower like–layered α-MnO_2/B@g-C3N4 nanocomposite for visible Light–Induced photocatalytic removal of tetracycline, Optical Materials. 136:113429. https://doi.org/10.1016/j.optmat.2022.113429

[22] Wei WR, Wang AN, Guo KH, He SX, Li AL, Kang XW, Fang JY (2022) Enhanced degradation of micropollutants by UV/freshly formed colloidal MnO_2: Reactive species, kinetics and pathways, Applied Catalysis B: Environmental. 313:121441. https://doi.org/10.1016/j.apcatb.2022.121441

[23] Du XR, Zou GJ, Wang ZH, Wang XL (2015) A scalable chemical route to soluble acidified graphitic carbon nitride: an ideal precursor for isolated ultrathin g-C_3N_4 nanosheets, Nanoscale. 7(19):8701-8706. https://doi.org/10.1039/c5nr00665a

[24] Shen GD, Pu YP, Cui YF, Jing PP (2017) Easy synthesis of TiO_2/g-C_3N_4 Heterostructure Photocatalyst with Large Surface Area and Excellent Photocatalytic Activity, Ceram Int. 43:S664-S670. https://doi.org/10.1016/j.ceramint.2017.05.243

[25] Dai X, Xie ML, Meng SG, Fu XL, Chen SF (2014) Coupled systems for selective oxidation of aromatic alcohols to aldehydes and reduction of nitrobenzene into aniline using CdS/g-C_3N_4 photocatalyst under visible light irradiation, Applied Catalysis B: Environmental. 158:382-390. https://doi.org/10.1016/j.apcatb.2014.04.035

[26] Landi SJr, Segundo IR, Freitas E, Vasilevskiy M, Carneiro J, Tavares CJ (2022) Use and misuse of the Kubelka-Munk function to obtain the band gap energy from diffuse reflectance measurements, Solid State Communications. 341:114573. https://doi.org/10.1016/j.ssc.2021.114573

[27] Tauc J, Grigorovici R, Vancu A (1966) Optical properties and electronic structure of amorphous germanium, Physica status solidi (b). 15(2):627-637. https://doi.org/10.1002/pssb.19660150224

[28] Li YF, Zhou MH, Cheng B, Shao Y (2020) Recent advances in g-C_3N_4-based heterojunction photocatalysts, Journal of Materials Science & Technology. 56:1-17. https://doi.org/10.1016/j.jmst.2020.04.028

[29] Wu L, Hu ML, Wang LP, Huang SM, Zhou XY (2023) Preparation of TiHAP@g-C_3N_4 Heterojunction and Photocatalytic Degradation of Methyl Orange, Journal of Inorganic Materials.

38(5):503-512. https://doi.org/10.15541/jim20220413

[30] Tsuruoka A, Isobe T, Matsushita S, Wakamura M (2015) A. Nakajima, Comparison of photocatalytic activity and surface friction force variation on Ti-doped hydroxyapatite and anatase under UV illumination, Journal of Photochemistry and Photobiology A-Chemistry. 311:160-165. https://doi.org/10.1016/j.jphotochem.2015.07.001

[31] Shang Q, Fang Y, Yin X, et al (2021) Structure modulation of g-C_3N_4 in TiO_2 {001}/g-C_3N_4 hetero-structures for boosting photocatalytic hydrogen evolution[J]. RSC advances, 11(59):37089-37102. https://doi.org/10.1039/d1ra07691d

[32] Panimalar S, Uthrakumar R, Selvi ET, Gomathy P, Inmozhi CK, Aviyarasu K, Kennedy J (2020) Studies of MnO_2/g-C_3N_4 hetrostructure efficient of visible light photocatalyst for pollutants degradation by sol-gel technique, Surf Interfaces. 20:100512. https://doi.org/10.1016/j.surfin.2020.100512

[33] Yu YZ Wang JG (2016) Direct microwave synthesis of graphitic C_3N_4 with improved visible light photocatalytic activity, Ceramics International. 42(3):4063-4071. https://doi.org/10.1016/j.ceramint.2015.11.078

[34] Vijayarangan R, Mohan S, Ilangovan R (2026) Intermediate-phase engineering in melamine-derived carbon nitride for enhanced visible light-driven photocatalysis, Surfaces and Interfaces. 98(26):110332. https://doi.org/10.1016/j.surfin.2026.110332.

[35] Nguyen VC, Pham ALH, Nguyen TD, Dreaml HDT, Pham THT, Nguyen TMT (2025) Bimetallic $MgFe_2O_4$@BiBTC hybrids for efficient photocatalytic degradation of rhodamine B， Nanoscale Advances. 7(23):7740-7753 https://doi.org/10.1039/d5na00774g

[36] Wang YT, Liu AR, Zheng Y, Song JY, Xian H, Jiang T (2024) Constructing carbon-vacancy introduced g-C_3N_4 coating ZIF-8 with strong adsorption performance and internal electric field for enhanced photodegradation, Surfaces and Interfaces. 46:104069. https://doi.org/10.1016/j.surfin.2024.104069

[37] Govindaraj T, Bharathi K, Kanagaraj C, Archana J, Navaneethan M (2026) Spin polarization and oxygen vacancy engineering in Mn-doped ZnCo2O4 spinels for enhanced photocatalysis, Journal of Environmental Chemical Engineering.14:120566.https://doi.org/10.1016/j.jece.2025.120566

[38] Muhammad YR, Rosari S, Ardiansyah T (2020) Characterization and photocatalytic activity

of Ag/Mn_3O_4/graphene composites under visible light irradiation for organic dyes degradation, Journal of Environmental Chemical Engineering. 8:103610. https://doi.org/10.1016/j.jece.2019.103610

Supplementary Files

This is a list of supplementary files associated with this preprint. Click to download.

- Highlights.docx
- TOC.png